

SUPPLEMENTARY INFORMATION

A. Experiment	14
1. Photonic and polaritonic states differ in the Floquet scheme	14
Polaritonic state observed in this work	15
2. Angular momentum mode sorting	16
3. Two-Photon Correlations	16
Angular Momentum Correlations	16
Spatial Correlations	17
4. Density matrix reconstruction	20
5. Experiment setup and typical sequence	20
6. Cavity details	22
7. Modes in the Lower Resonator Waist	24
8. Electric field management	24
B. Theory	25
1. Collective atomic excitations	25
2. Floquet polaritons are protected from intracavity aberrations	26
3. Many-body spectrum	28
4. Varieties of Two-Particle Laughlin States	28
5. Collision analysis	29
6. Understanding the Width of the Energy-Conservation Feature	30

Supplement A: Experiment

1. Photonic and polaritonic states differ in the Floquet scheme

When forming dark polaritons in a set of near-degenerate cavity modes whose bare frequencies are all close to that of the unmodulated atomic transition, the relationship between photons and polaritons is independent of the mode. For example, because the atom-cavity coupling g_l is the same for each mode l , the dark-state rotation angle θ_l is the same for every mode, where the rotation angle satisfies $\tan(\theta_l) \equiv g_l/\Omega$ (see [32] and SI B5 of Ref. [18]). A smaller ratio g_l/Ω increases the contribution $\cos^2(\theta_l)$ to the polaritons from the cavity photon and thus makes the polariton more “photon-like”; a larger ratio increases the contribution $\sin^2(\theta_l)$ from the collective Rydberg state, making the polariton more “Rydberg-like” [32]. Therefore, when using a set of nearly-degenerate bare cavity modes, all of the polaritons have the same fractional composition in terms of their photonic and Rydberg parts so long as the atomic density and Rydberg coupling fields are uniform over all modes.

The Floquet scheme causes the dark-state rotation angle, and thus the polariton composition, to vary between different modes. The rotation angle varies because the so-called “sideband” features with $l = 3 \& 9$ have smaller atom-cavity coupling than the “carrier” with $l = 6$. For

the parameters used in this work, the sideband dark polaritons are approximately eight times more photon-like than the carrier polaritons.

The second difference between polaritons and photons in the Floquet scheme arises from the complex phase of g_l and is more subtle to understand. Before considering the phases of the couplings, it is helpful to use a concrete example of the effect of the phase on a superposition of angular momentum states. For concreteness, consider the collective Rydberg states $|R_{\pm}\rangle = \frac{1}{\sqrt{2}}(r_3^\dagger \pm r_6^\dagger)|vac\rangle$. These Rydberg excitations form angular standing waves because of the interference between the $l = 3$ and $l = 6$ components; but the probability wave peaks of $|R_+\rangle$ match the troughs of $|R_-\rangle$, and vice versa, because of the flipped phase of the superposition. When utilizing ordinary polaritons with a constant $g_l \equiv g$, $|R_{\pm}\rangle$ couple with cavity photonic states $|a_{\pm}\rangle = \frac{1}{\sqrt{2}}(a_3^\dagger \pm a_6^\dagger)|vac\rangle$, where the peaks of $|a_+\rangle$ ($|a_-\rangle$) are at the same locations as the peaks of $|R_+\rangle$ ($|R_-\rangle$). Similar considerations apply for states containing multiple excitations; for ordinary polaritons, the spatial structures of the Rydberg components and the photonic components are the same.

In the Floquet scheme, the structure of the single photon state $|\tilde{a}_{\pm}\rangle \propto (a_3^\dagger \pm \frac{g_3}{g_6}e^{2\pi i f_{\text{mod}} t}a_6^\dagger)|vac\rangle$ which couples to $|R_{\pm}\rangle$ is different in three important ways. First, the magnitude $\left|\frac{g_3}{g_6}\right|$ of the ratio between the coupling strengths determines the relative weights of the parts of the photonic superposition. Second, the relative phase $\arg\left(\frac{g_3}{g_6}\right)$ of the couplings affects the relative phase of the photonic superposition. When using sinusoidal Floquet modulation, the phases satisfy $\arg\left(\frac{g_3}{g_6}\right) + \arg\left(\frac{g_9}{g_6}\right) = \pi$. Third, in the lab frame the phase of the superposition rotates at the modulation frequency f_{mod} . As a result, the positions of peaks and troughs in the probability wave will rotate around the center of the cavity at frequency $f_{\text{mod}}/3$, where the factor of three arises because of the angular momentum difference between the modes in the superposition (equivalently, the fact that the density wave has three peaks). This rotation can be viewed as the micromotion which is quite common in Floquet systems.

In this work, the two-Rydberg component of the polaritonic state produced by interactions is approximately,

$$|R_L\rangle \propto \left(\sqrt{\frac{21}{10}} \left| \frac{g_3 g_9}{g_6^2} \right| r_3^\dagger r_9^\dagger - \frac{1}{\sqrt{2}} (r_6^\dagger)^2 \right) |vac\rangle,$$

noting that the factor $1/\sqrt{2}$ simply cancels a factor from the bosonic creation operators $(r_6^\dagger)^2$. The factor $\sqrt{21/10}$ is explained in SI B 4. As a result of the Floquet scheme,

this Rydberg state couples to a two-photon state,

$$\begin{aligned} |\tilde{a}_A\rangle &\propto \left(\sqrt{\frac{21}{10}} e^{i \arg(g_3 g_9 / g_6^2)} a_3^\dagger a_9^\dagger - \frac{1}{\sqrt{2}} (a_6^\dagger)^2 \right) |vac\rangle \\ &\propto \left(\sqrt{\frac{21}{10}} a_3^\dagger a_9^\dagger + \frac{1}{\sqrt{2}} (a_6^\dagger)^2 \right) |vac\rangle. \end{aligned}$$

Two key features of this photonic state are worth noting: First, because the rotation factors at $\pm f_{\text{mod}}$ from the $l = 3$ and $l = 9$ photons in the first term on the right-hand side cancelled out, there is no time-dependence of the Laughlin state itself. Even though all photonic states in the Floquet scheme rotate at $f_{\text{mod}}/3$, the rotation-invariance of the Laughlin state prevents it from acquiring time-dependence. However, the net phase factors from the sideband couplings relative to the carrier do not cancel out; they contribute a factor $e^{i \arg(g_3 g_9 / g_6^2)} = -1$ which causes the photonic superposition to have a plus sign rather than a minus sign. In SI A3 we discuss the use of the phase compensation cavity to convert the state $|\tilde{a}_A\rangle$ which exits the science cavity into the photonic Laughlin state,

$$|\tilde{a}_L\rangle \propto \left(\sqrt{\frac{21}{10}} a_3^\dagger a_9^\dagger - \frac{1}{\sqrt{2}} (a_6^\dagger)^2 \right) |vac\rangle.$$

While rotation-invariance makes the Laughlin state $|\tilde{a}_L\rangle$ time-independent, the rotation induced by the Floquet scheme plays a crucial role when measuring spatial correlations. The off-center single mode fiber measures localized photons; when viewed in the angular momentum basis, the localized fiber mode has an annihilation operator corresponding to a superposition $a_f \propto c_3 a_3 + c_6 a_6 + c_9 a_9$ where c_l is the coefficient characterizing the contribution from mode l . When the fiber is translated to the radius with peak density, the coefficients are approximately $c_3 = 0.53$, $c_6 = 0.71$, and $c_9 = 0.46$. Immediately after a photon from the Laughlin state is detected through the single mode fiber, the remaining photon is in the state,

$$\begin{aligned} |\tilde{a}_{\text{rem}}\rangle &\propto a_f |\tilde{a}_L\rangle \\ &\propto \left(\sqrt{\frac{21}{10}} (c_9 e^{-2\pi i f_{\text{mod}} t} a_3^\dagger + c_3 e^{2\pi i f_{\text{mod}} t} a_9^\dagger) \right. \\ &\quad \left. - \sqrt{2} c_6 a_6^\dagger \right) |vac\rangle. \end{aligned}$$

Because the remaining photon is left behind in a state with spatial structure which is not rotation-invariant, the probability distribution of the remaining photon rapidly rotates in space. Immediately after the first photon is detected, the remaining photon has no overlap with the fiber mode and will not be observed; just half of a rotation period later the likelihood of detecting the photon

is maximized. In particular, the likelihood of observing the second photon through the fiber follows,

$$\langle \tilde{a}_{\text{rem}} | a_f^\dagger a_f | \tilde{a}_{\text{rem}} \rangle \propto \sin^4(2\pi f_{\text{mod}} t).$$

Polaritonic state observed in this work

Due to the finite lifetime and interaction strength of the polaritons, in this work pairs of polaritons form a Laughlin-like correlated state but not a pure Laughlin state. The primary difference between the polaritonic state and a Laughlin state is an excess of polariton population in $|66\rangle$. Qualitatively, this excess arises because the probe laser couples the system from $|6\rangle$ to the polariton pair state $|66\rangle = \sqrt{\frac{10}{31}} |L\rangle + \sqrt{\frac{21}{31}} |AL\rangle$. In the ideal case, the interaction-induced shift and decay of the anti-Laughlin state $|AL\rangle$ is sufficient to completely suppress its injection into the cavity, resulting in the excitation of a pure polaritonic Laughlin state $|L\rangle$. In the non-ideal case of the actual experiments, the shift and decay of $|AL\rangle$ relative to $|L\rangle$ are finite, resulting in a polaritonic state which has an enhanced Laughlin component but still an excess of $|66\rangle$ relative to the pure Laughlin state. We describe this polaritonic state as “Laughlin-like” because it still shares key physical features with the Laughlin state. In particular, it arises because of strong interactions between particles in a synthetic magnetic field. Moreover, the polaritons in this state still avoid each other. Starting from our observation that photons avoid each other by $A_{\text{phot}} = 1 - (g^{(2)}(\phi=0) / \int d\phi g^{(2)}(\phi)) = 73(34)\%$, meaning that they are A_{phot} less likely to be in the same location than they are to be at a random angular separation around the ring, we can account for the fact that $l = 3$ & 9 polaritons are approximately eight times more photon-like than those with $l = 6$ to determine that the Rydberg components (which dominate the polariton population) avoid each other by $A_{\text{pol}}=17(9)\%$. While this result uses the complete form of the polariton wavefunction, we note that because the avoidance arises from the cross-term between the $|39\rangle$ and $|66\rangle$ components of the wavefunction, $A_{\text{pol}}/A_{\text{phot}} \approx 2 \left| \frac{g_3 g_9}{g_6^2} \right| = 1/4$.

While perfect spatial antibunching of polaritons would dramatically reduce the anti-bunching in $g_{66}^{(2)}$, our numerics based on non-Hermitian perturbation theory (see SI B9 of Ref. [18]) indicate that under our current conditions the value of $g_{66}^{(2)}(0)$ shown in Fig. 3d would only be approximately 20% lower if the angular momentum modes $l = 3$ & 9 were inaccessible.

The lifetime and interaction strength of cavity Rydberg polaritons are complicated functions of many factors [74], but the overall performance of these polaritons for many-body physics is primarily limited by the collective cooperativity in each mode [17, 18, 75]. The cooperativity in our system is impacted by the Floquet scheme. In

the present setup the total atom-cavity coupling strength is typically $g = 2\pi \times 15$ MHz, the total Rydberg coupling strength is $\Omega = 2\pi \times 1.8$ MHz, and the empirical collective Rydberg decay rate is $\Gamma_R = 2\pi \times 40$ kHz. The Floquet scheme requires us to split the atom-cavity coupling strength g among the different modes, such that $g \approx \sqrt{g_3^2 + g_6^2 + g_9^2}$, resulting in the performance observed in this work; it also yields a shared Rydberg coupling strength of $\Omega = 2\pi \times 1.4$ MHz for every mode. If our cavity were free from the intracavity aberrations which require us to form the Landau level with the Floquet scheme (SI B 2), then we could tune the cavity to a length at which the cavity modes comprising the Landau level would be directly degenerate. According to our simulations via non-Hermitian perturbation theory (see SI B9 of Ref. [18]), under that condition the present coupling strengths of the system would be sufficient to form polaritonic Laughlin states with a fidelity of 75% and a spatial avoidance of 50%. Reasonable increases in atomic density and cavity finesse will enable even further improvement in these figures of merit in the future.

2. Angular momentum mode sorting

To perform detection of photons in angular momentum space we utilize the mode sorting setup depicted in Fig. 2a. The key elements in this setup are the mode filters, each consisting of a tunable two mirror non-degenerate cavity. These filter cavities are independently locked to a 795 nm laser with tunable frequency offsets, such that we can match the frequency of the filter cavity mode with angular momentum l to the frequency of the photons exiting the science cavity with the same angular momentum. The three cavities differ slightly in their parameters, but the typical cavity is composed of two identical mirrors with 98.7% transmission and radii of curvature $R = 10$ m at a separation of 15 cm, yielding a linewidth of $\kappa_{\text{filt}} = 2\pi \times 4$ MHz and a transverse mode spacing of 55 MHz. Because the science cavity angular momentum modes are separated by $f_{\text{cav}} \approx 70$ MHz much greater than the filter cavity linewidth, the filters are able to discriminate between the science photons using both their spatial mode structure and their frequency. Each cavity transmits all superpositions of TEM_{pq} modes with $p+q = C$ constant, and the integer C determined by the resonator length—this makes the mode-sorting cavities insensitive to the astigmatism of the photons induced by reflection/refraction off of the resonator mirrors as the photons leave the twisted physics cavity.

The typical mode sorting/filter cavity has a net transmission of 40% for photons with the desired mode structure (orbital angular momentum in the lower waist of the resonator) and suppresses transmission of photons with the wrong angular momentum by a factor of 2000. The transmission of each mode sorting cavity is routed to a

unique single photon counting module by a multimode fiber.

The experiments reported in Fig. 2 of the main text were performed using all three mode sorting cavities simultaneously, with each cavity tuned to transmit a different angular momentum mode. The experiments reported in Fig. 3 were performed before the third mode sorting cavity was constructed. Therefore, the data shown in Fig. 3d were collected in separate experiment runs from the data in Fig. 3e; in between, the two mode sorters were adjusted to transmit the relevant angular momentum modes.

3. Two-Photon Correlations

We characterize the light exiting the science cavity using two-photon correlation functions,

$$g_{jk}^{(2)}(\tau) = \frac{\langle n_j(t)n'_k(t+\tau) \rangle_t}{\langle n_j \rangle \langle n'_k \rangle}, \quad (\text{S1})$$

between the photons $n_j(t)$ in mode j counted at a first detector and $n'_k(t)$ in mode k counted at a second detector, where the angle brackets denote time averaging and τ is the time delay between the detection events. The mode labels j and k may represent angular momentum modes with $l = j$ and $l = k$, or they may represent the spatially localized mode of the single-mode fiber. When $j = k$, we typically use a beam splitter to divide the photons between two separate single photon counting detectors. For many of our measurements the background count rates in the absence of the probe are comparable to the signal rates in the presence of the probe; the correlation functions presented in this work correspond to the correlations of signal photons with the backgrounds removed, as detailed in SI A2 of Ref. [18].

Angular Momentum Correlations

The correlation functions presented in the main text Fig. 3c-e were collected during three separate runs of the experiment. In the first run (Fig. 3c), a multi-mode fiber splitter was used to collect all of the photons exiting the science cavity, regardless of mode, and split them evenly between two single photon counters. In the second run (Fig. 3d), the first mode sorting filter was tuned to transmit half of the photons in $l = 6$, while the second mode sorting filter transmitted the remaining half of photons with $l = 6$. In the third run (Fig. 3e), the first mode sorting filter transmitted photons with $l = 9$ and the second filter transmitted photons with $l = 3$.

The two-photon population fractions shown in Fig. 3f of the main text for $j = k = 6$ and $j = 3, k = 9$ are calculated by comparing the observed coincidence rates

as,

$$\frac{\rho_{ij}}{\rho_{\text{tot}}} = \frac{\langle n_j(t)n'_k(t) \rangle_t}{\langle n_{mm}(t)n'_{mm}(t) \rangle_t} \frac{2}{(1 + \delta_{jk})\xi_j\xi'_k}, \quad (\text{S2})$$

where n_{mm} (n'_{mm}) is the signal at the first (second) output port of the multimode splitter used to measure $g_{\text{all}}^{(2)}(\tau)$, ξ_j (ξ'_k) is the mode-sorted detection efficiency for mode j (k) on the first (second) detector relative to the efficiency of a single output port of the multimode splitter, and δ_{jk} is the Kronecker delta. Each of the detection efficiencies is independently calibrated by probing on the relevant dark polariton resonance and comparing the count rate after the mode-sorting filter to the count rate after the multimode splitter. Let $N_{jk}(\tau) = \langle n_j(t)n'_k(t+\tau) \rangle_t$ be the observed rate of two-photon events separated by time τ . For the mode-sorted cases we estimate $N_{jk}(0)$ by fitting the observed delay-time-dependent $N_{jk}(\tau)$ and extracting the zero-delay value from the fit; empirically, we find that $N_{39}(\tau)$ is well fit by a Lorentzian and $N_{66}(\tau)$ is well fit by the solution to the optical Bloch equations for a two-level system (see Ref. [18] SI A2). For the multimode case we do not have a suitable fitting function, and therefore we directly use the observed value $\int_{-\Delta/2}^{\Delta/2} d\tau N_{mm}(\tau)$ averaged over a time bin with width $\Delta = 600$ ns around zero delay.

We find that the observed populations ρ_{39} and ρ_{66} may not fully account for the observed coincidences in the multimode data, with $\frac{\rho_{39}+\rho_{66}}{\rho_{\text{tot}}} = 0.85(15)$. Since we do not directly measure the correlations in any other combinations of angular momentum modes, Fig. 3f uses the estimate that the remaining population fraction of 0.15(15) is split evenly among the remaining mode pairs. The actual distribution of this additional population among the four possible mode pairs does not affect any of our conclusions, including the density matrix and the overlap of the observed state with the Laughlin state as discussed in SI A 4. Physically, we note that angular momentum conservation should prevent these other mode pairs from being populated at all; however, we are not able to place any further constraints on their populations based on our measurements. Note also that our use of a weak probe beam, as well as the strong interaction-induced blockade of all three polariton states among these three modes, should make the effect of three-photon states on these results negligible.

Spatial Correlations

We perform measurements in real space using a single mode fiber. To properly align the fiber to detect photons in the Landau level at the desired position, we first choose an asphere as well as the position and angle of the fiber which maximizes the coupling of $l = 0$ photons from the cavity into the fiber. Once that coupling is optimized, we

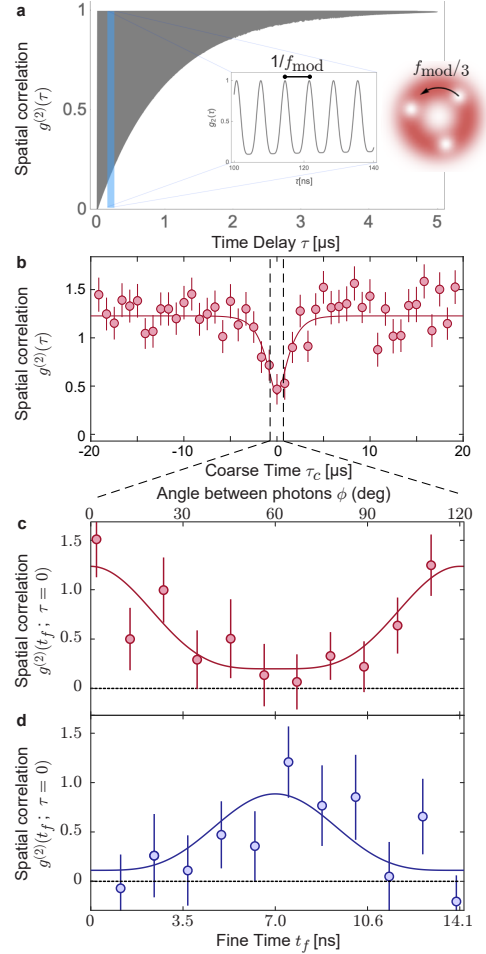


FIG. S1. Extracting angular correlations from rapidly rotating second photon. **a**, Illustration of the correlation function measured through a single mode fiber. Oscillation in the signal at f_{mod} arises from the wavefunction of the second photon, which has three holes whose positions are determined by that of the first detected photon and which rotate at $f_{\text{mod}}/3$ (inset). The rotation decays over a microsecond timescale containing hundreds of rotation periods. **b**, Viewed in coarse time τ_c with averaging over a timescale much longer than the rotation period, the correlations exhibit ordinary anti-bunching. Solid curve guides the eye. **c**, Breaking up the central point into 11 parts based on their fine time t_f within the rotation period reveals the oscillating correlations. The instantaneous correlation ($t_f = 0$) corresponds to the same-location correlation ($\phi = 0$), while half a period later we see the correlations between locations separated by $\phi = 60^\circ$. Without the phase compensator, we observe photon bunching at $t_f = 0$. **d**, With the phase compensator, photons are anticorrelated at $t_f = 0$. Solid curves show fits based on (c) Eq. S5 and (d) Eq. S4. Error bars show standard error.

use a four-axis stage (two-dimensional translation, tip, and tilt) to perform a “magnetic translation” of the fiber tip [19]. In particular, we send $l = 6$ photons through the cavity and repeatedly adjust the position and angle of the fiber until the fraction of $l = 6$ photons entering

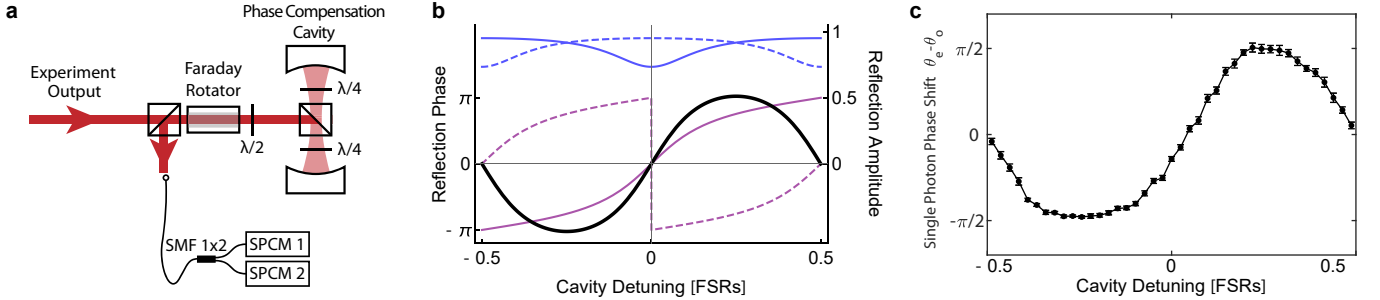


FIG. S2. Phase compensation cavity for spatial correlation measurements. **a**, To compensate for the additional phase shift of the photons relative to the polaritons which is induced by the Floquet scheme, we send the light emitted from the main science cavity (“experiment output”) to a phase compensation cavity (PCC), which contains two quarter waveplates and a polarizing beam splitter cube that can be used to tune its finesse. Almost all of the light is reflected from the PCC after experiencing the desired phase shift. It subsequently travels to the single mode fiber, where it is split and sent to two separate single photon counting modules (SPCM) for correlation measurements. **b**, The PCC is a confocal cavity with 82% effective transmission of the first mirror (determined by the waveplate angle), 0% transmission of the second, and 12% intracavity loss. While all modes experience relatively little loss (blue, top), even modes (solid) reflected from the cavity experience a different phase shift (purple) than odd modes (dashed). The net phase shift for the two-photon states $|66\rangle$ relative to $|39\rangle$ (black solid) can be tuned over 2π by changing the cavity length. **c**, Experimental calibration in the *single-photon sector* verifies a tunable phase shift of up to $\pm\pi/2$ for even modes relative to odd modes. The vertical scale of the phase variation in this panel (c) is half that of the previous panel (b) because it is a measurement of the *single photon* shift, rather than the two photon shift.

the fiber is maximized. This process matches the fiber to a magnetically translated Gaussian in our lowest Landau level at a radius near the peak in the average density of photons that are exiting the cavity in pairs (as depicted in Fig. 4b).

Ordinarily, a single fiber would only be able to reveal the correlations at that single location. However, as discussed in SI A 1, immediately after a first photon is detected through the single mode fiber, the Floquet scheme used in this work causes the second photon to rotate one third of the way around the ring with a temporal period of $T_{\text{mod}} = 1/f_{\text{mod}} = 14$ ns which is much faster than other dynamical timescales of the system. Note that any wavefunction in our Landau level has an azimuthal periodicity of $2\pi/3$, and therefore rotating one third of the way around the ring is sufficient to map the wavefunction back on to itself. Therefore, the correlations between photons in the single mode fiber separated by a “fine time” $t_f = \tau \bmod T_{\text{mod}}$ are equivalent to the angular correlations that would be observed between photons at equal time with angular separation $\phi_f = \frac{2\pi}{3} \frac{t_f}{T_{\text{mod}}}$,

$$g^{(2)}(\phi_f; \tau = 0) = g_{ff}^{(2)}(t_f). \quad (\text{S3})$$

An illustration of this behavior is provided in Fig. S1a.

Therefore, to characterize the angular correlations, we perform high resolution measurements of photon arrival times through the single optical fiber. After entering the single-mode fiber, we split the field into two halves and send each to a single photon counting module. We use a home-built FPGA-based photon time tagger with 1.4 ns resolution to characterize the photon arrival times. We convert the temporal correlations $g_{ff}^{(2)}(t_f)$ into the cor-

relation function $g^{(2)}(\phi, \tau = 0)$ using Eq. S3. Since we are unable to collect sufficient statistics to characterize correlations during a single rotation period, we instead average data corresponding to the same fine time t_f over many rotation periods within a large “coarse time” bin of total duration 1.2 μ s. The result of this process is depicted in Fig. S1b & c. To calibrate any additional time offset due to time delay differences in the two detection paths, we perform a separate set of measurements sending rapidly intensity modulated coherent light directly into the fiber splitter; we extract the time delay as the difference in measured arrival times for peaks and troughs of that signal along the two detection paths. That time delay calibration has been accounted for in Fig. S1c & d, such that the correlation signal at $t_f = 0$ properly corresponds to photons arriving at the fiber tip at the same time.

As explained in SI A 1, our Floquet scheme induces a shift of π in the relative phase between $|66\rangle$ and $|39\rangle$ in the photonic state relative to the polaritonic state. As a result, a spatial correlation measurement performed directly after the science cavity reveals photon bunching at $t_f = 0$ ($\phi = 0$), as shown in Fig. S1c. While this phase shift can be compensated with a linear optical transformation, it is not affected by diffraction, single lenses, or single mirrors, and thus must be manipulated with a slightly more sophisticated “optical element”.

In order to compensate for this phase and produce a photonic Laughlin state, we implement the phase compensation cavity (PCC) depicted in Fig. S2a. The PCC consists of two curved mirrors with an intracavity polarizing beam splitter and quarter waveplates which can be used to tune the effective reflectivity of the mirrors.

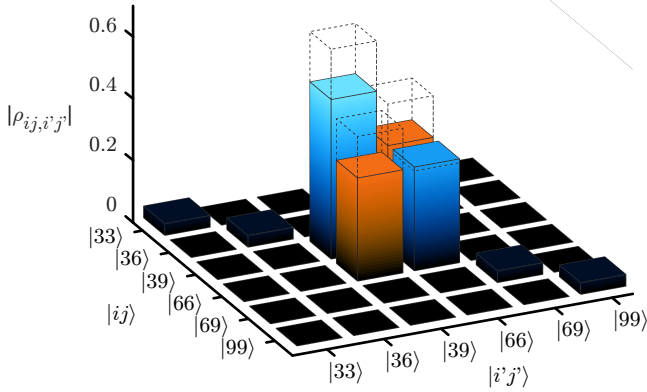


FIG. S3. Density matrix in the two-photon sector. Combining our results in real space (Fig. 4) and angular-momentum space (Fig. 3) enables us to reconstruct the density matrix of the two-photon state which exits our system (solid bars). Blue bars are positive, orange bars are negative. Dashed bars correspond to the pure Laughlin state.

We adjust the waveplates to make the PCC behave as a single-ended cavity with 82% transmission on the input coupler, maximum reflection on the output coupler, and 12% intracavity loss; this corresponds to an overall finesse of 3. Moreover, we adjust the length of the cavity to be near-confocal, so that all even modes are degenerate and all odd modes are degenerate. While nearly all of the light incident upon the PCC is reflected regardless of its parity or frequency, the PCC induces a tunable, parity-dependent phase shift (Fig. S2b). We chose the finesse of the cavity so that the phase shift per photon for even modes relative to odd modes is $\pi/2$ over a wide range of cavity detunings (Fig. S2c), and we then lock the cavity in the center of that range.

Because $|66\rangle$ contains two even-parity photons and $|39\rangle$ contains two odd-parity photons, reflecting from the PCC induces a total relative phase shift of π between them. Therefore, it exactly compensates for the extra phase induced by the Floquet scheme. As a result, when we reflect the light exiting the science cavity off of the PCC before performing the spatial correlation measurement, we observe the anti-bunching at time $t_f = 0$ ($\phi = 0$) which is characteristic of the Laughlin state (Fig. S1d).

We have performed a thorough statistical analysis to test the significance of the oscillating correlations shown in Fig. S1. First, as discussed in the main text, we fit the observed correlations shown in Fig. S1d with the empirical function,

$$g_{\text{fit}}^{(2)}(\phi) = g_0 + g_1 \sin^4(3\phi/2) \quad (\text{S4})$$

which allows for an offset g_0 from perfect spatial anti-bunching and a reduction of the oscillation amplitude g_1 due to imperfect state fidelity or detection. The fit yields a small offset $g_0 = 0.11(19)$ and an oscillation amplitude $g_1 = 0.77(36)$ with a significance of 2.1 standard devia-

tions corresponding to a probability of 0.02 to arise from statistical fluctuations in a system with no dependence of correlation on angle. The quoted errors for the fit parameters are calculated using the standard approach of error propagation [79]. That is, we first note that the parameter estimate $g_1 = f_1(g_j^{(2)})$ arises from a least squares fitting procedure f_1 based on the observed correlation datapoints $g_j^{(2)}$ with standard errors σ_j where j is an index running from one to eleven because we have eleven data bins. The error in the fit parameter $\sigma_{g_1} = \sqrt{\sum_j \left(\frac{\partial f_1}{\partial g_j^{(2)}} \right)^2 \sigma_j^2}$ is thus determined by the dependence of the results of the entire fitting procedure on the variations in the measured data. Further note that the quoted probability corresponds to a one-sided statistical test, since an oscillating correlation with the opposite trend ($g_1 < 0$) would not be regarded as coming from the spatial anti-bunching of a Laughlin state.

Our confidence in this result is further bolstered by accounting for additional data taken without phase compensation shown in Fig. S1c. The physics tested by this dataset is expected to be essentially the same as that tested by the phase compensated data; the only difference should be the π phase shift of the superposition, resulting in the observation of spatial bunching (equivalently, a bunching signal at time zero) instead of anti-bunching. As a result, we fit the observed correlations without phase compensation using the function,

$$g_{\text{uncomp}}^{(2)}(\phi) = g_0 + g_1 \cos^4(3\phi/2) \quad (\text{S5})$$

which accounts for the π phase shift by replacing sin with cos. In principle, the parameters g_0 and g_1 appearing in Eqs. S4 & S5 which characterize the oscillations should take the same values. Indeed, for the uncompensated data we obtain $g_0 = 0.20(13)$ and $g_1 = 1.04(28)$ which are within one standard deviation of the values quoted above in the phase compensated case. If we consider these to be two measurements of the same quantity and calculate the overall maximum likelihood estimate of the oscillation amplitude, we obtain $g_1 = 0.94(22)$ with a significance of 4.3 standard deviations corresponding to a probability of 9×10^{-6} to arise from statistical fluctuations in a system with no dependence of correlation on angle, as quoted in the main text.

We also perform a low power, naïve statistical test which ignores the time-ordering of the data as well as our physical expectations to simply ask: *is the un-phase-compensated data (with higher SNR) likely to arise from 11 independent measurements of an underlying constant correlation $g^{(2)}$?* Even here we find that the probability of our observations arising from such statistical fluctuations is only 1.7%. This test has the advantage of not relying upon *any* knowledge of the underlying physics or even the time-ordered nature of the measurement, but the disadvantage of being substantially less sensitive than

the previous tests.

4. Density matrix reconstruction

Here we combine the results of our measurements in angular momentum space and real space to calculate the density matrix among the two-photon states in our system, which has the elements,

$$\rho_{ij,i'j'} = \langle ij | \rho | i'j' \rangle. \quad (\text{S6})$$

The calculation of the diagonal elements $\rho_{39} \equiv \rho_{39,39}$ was discussed in SI A 3 with the results shown in the main text Fig. 3f.

We determine the relevant off-diagonal density-matrix element $\rho_{39,66}$ based on the observed spatial correlations. The angular correlation function of the ideal Laughlin state is,

$$\begin{aligned} g^{(2)}(\phi) &= \frac{8\bar{g}}{3} \sin^4(3\phi/2) \\ &= \bar{g} \left(1 + \frac{1}{3} \cos 6\phi - \frac{4}{3} \cos 3\phi \right), \end{aligned}$$

where \bar{g} is the time-averaged correlation. With an arbitrary density matrix among the states $|39\rangle$ and $|66\rangle$, the correlation function takes the form,

$$\begin{aligned} g^{(2)}(\phi) &= \bar{g} \left(\frac{651}{260} \rho_{66} + \frac{155}{546} \rho_{39} (1 + \cos 6\phi) \right. \\ &\quad \left. - \frac{124}{\sqrt{1890}} \Re(\rho_{39,66}) \cos 3\phi \right). \quad (\text{S7}) \end{aligned}$$

This form is independent of the radius at which the single mode fiber is placed. We fit the spatial correlation data shown in Fig. S1d with Eq. S7 and use the separately measured populations ρ_{66} and ρ_{39} to extract the coherence $\rho_{39,66} = -0.33(16)$.

Note that Eq. S7 neglects the additional possible contributions to the average value which come from the population in other angular momentum pair states ($|33\rangle$, $|36\rangle$, etc.). Because these contributions depend more sensitively on the position of the fiber, and because we do not know how the additional 15% of the population is distributed among these pair states, we take the most conservative approach and neglect their contributions entirely. This approach is conservative because it yields the smallest magnitude of $\rho_{39,66}$ and therefore the smallest inferred overlap with the Laughlin state. Note also that because only the real part of the coherence $\Re(\rho_{39,66})$ contributes to the observed correlations, we cannot distinguish between a loss in magnitude of $\rho_{39,66}$ and the presence of an imaginary component. We treat our results as if there is no imaginary component; however, this choice does not affect the inferred overlap with the Laughlin state below.

An additional subtlety arises because our optics for collecting photons leaking out of the cavity are imagining the field at the upper cavity waist, rather than the lower cavity waist, onto the plane of the single mode fiber. While the transverse profiles of the cavity modes at the lower waist correspond closely to the wavefunctions of an ideal lowest Landau level, their form in the upper waist is somewhat distorted (see Fig. S6). As a result, the localized mode in the upper waist admitted by our single mode fiber only corresponds to an *approximately* localized mode in the lower waist. This fact has two primary consequences: 1. the expected form of the spatial correlation function is no longer entirely independent of the transverse position of the fiber and 2. the measured correlation $g^{(2)}(\phi = 0)$ between photons at the same location no longer generically drops to zero even for a perfect Laughlin state. We estimate that for the actual alignment of our single mode fiber the minimum possible correlation that we could have measured for an ideal Laughlin state is $g^{(2)}(\phi = 0)/\bar{g} = 0.03$; this value is relatively small compared to the experimentally observed $g^{(2)}(\phi = 0)/\bar{g} = 0.3(2)$, indicating that the difference between detection in the lower and upper cavity waists is likely negligible under our current conditions. When calculating the density matrix, we use the conservative assumption that the observed incomplete contrast is caused entirely by a state with imperfect off-diagonal coherence rather than a state with greater off-diagonal coherence measured with an imperfect apparatus.

Our final result for the density matrix based on these conservative assumptions is shown in Fig. S3. This density matrix has a “Laughlin fidelity”, its overlap with the pure Laughlin state, of,

$$F = \langle L | \rho | L \rangle = 76(18)\%, \quad (\text{S8})$$

as reported in the main text.

Alternatively, we can calculate the Laughlin fidelity under an optimistic set of assumptions. In particular, because this system should satisfy angular momentum conservation, we can assume that there is actually no population in the other angular momentum pair states; in that case we set $\rho_{33} = \rho_{36} = \rho_{69} = \rho_{99} = 0$, and we re-scale the populations in the remaining two states such that their ratio matches our experimental observations but their sum is $\rho_{66} + \rho_{39} = 1$. If we also recalculate the off-diagonal coherence under those assumptions, then the resulting density matrix corresponds to an optimistic Laughlin fidelity of 90(18)%.

5. Experiment setup and typical sequence

Our experiments begin with a gas of 10^7 cold ^{87}Rb atoms at a temperature of 15 μK prepared using a magneto-optical trap and polarization gradient cooling (Fig. S4a). We transport that gas vertically into the

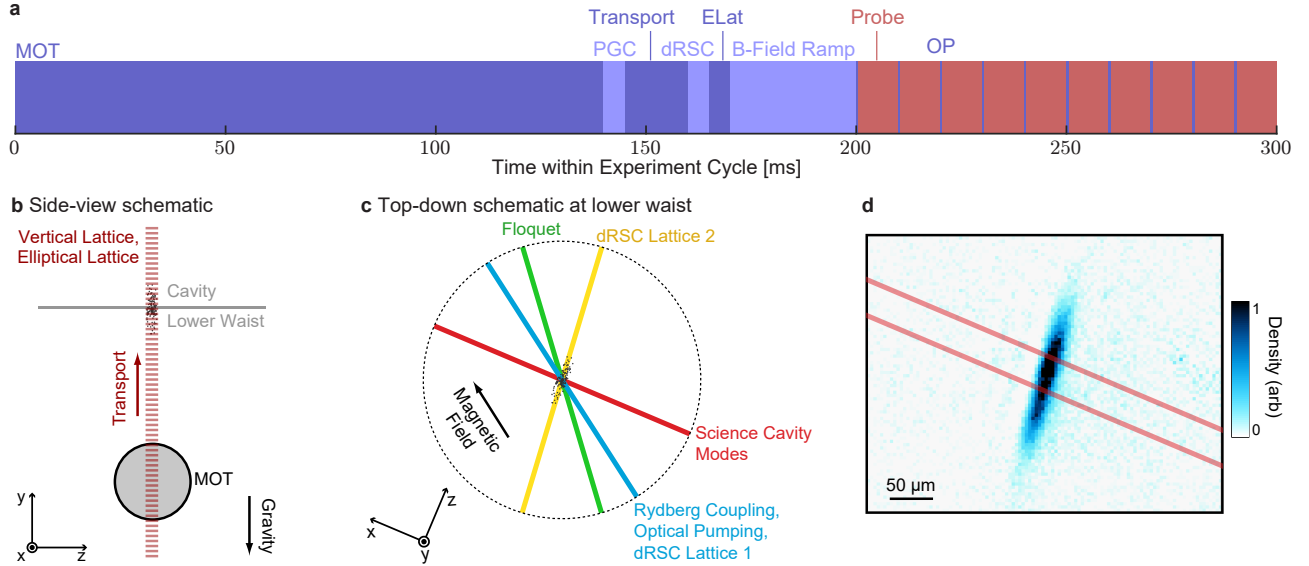


FIG. S4. Experiment sequence and schematics. **a**, Our typical experiment sequence repeats every 300 ms. It begins with loading of the magneto-optical trap (MOT) while the electronic control system prepares to execute the rest of the sequence, followed by polarization-gradient cooling (PGC), transport of the atoms from the MOT to the cavity using a moving, vertical optical lattice (VLat), degenerate Raman sideband cooling (dRSC), transfer of the atoms into an elliptical optical lattice (ELat) to reshape the cloud, a ramp of the bias magnetic field and settling time to ensure stability, and finally ten, ~ 10 ms probe cycles separated by brief pulses of optical pumping (OP) light. **b**, A schematic of the experiment shown from the side, indicating beam alignment. **c**, A schematic of the experiment from a top-down perspective, indicating the four beam paths which cross at the lower waist of the science cavity, as well as the beam(s) which propagate along each path. The bias magnetic field is parallel to the Rydberg coupling axis. **d**, An example image of the atomic cloud after transfer into the ELat, which is wide transverse to the cavity mode but narrow along the cavity z -axis. The red lines indicate the edges of the fundamental mode of the science cavity.

waist of our science cavity using a moving optical lattice (Fig. S4b). Previous iterations of the experiment would then release the gas from the trap in order to prevent inhomogeneous broadening of the ground to Rydberg transition due to the trapping beams [17, 18]. To improve the atomic density and experiment duty cycle for these experiments, we now cool the gas to a temperature below $1 \mu\text{K}$ and polarize the atoms into the lowest energy spin-state $|F = 2, m_F = -2\rangle$ within the hyperfine manifold $F = 2$ using degenerate Raman sideband cooling [77]. We then transfer the gas into an elliptical dipole trap, which we retroreflect to form an optical lattice in order to support the atoms against gravity. This trap makes the gas at the cavity waist highly elliptical, with a very thin root-mean-squared (RMS) radius of $11 \mu\text{m}$ along the science cavity axis (\hat{z}) which makes the polariton interactions strong [17] while maintaining much larger transverse RMS radii of $51 \mu\text{m} \times 120 \mu\text{m}$ in order to cover the area spanned by the desired transverse modes of the cavity (Fig. S4d).

The elliptical lattice primarily traps the ground state atoms and only slightly perturbs the Rydberg state, resulting in an AC Stark shift of the two-photon resonance frequency for the $5S_{1/2} \rightarrow 111D_{5/2}$ transition of each atom. These shifts lead to inhomogeneous broadening

because atoms at different positions in the trap experience different potentials. However, because the sample temperature (and therefore the spread of Stark shifts) of less than $1 \mu\text{K}$ corresponds to a frequency scale of less than 20 kHz , this inhomogeneous broadening makes a tolerably small contribution to the observed Rydberg linewidth of $\Gamma_R = 2\pi \times 50 \text{ kHz}$. Therefore, we are able to leave the elliptical lattice on throughout the probe cycle in which we create dark polaritons.

We have found that careful management of the polarizations of the atoms and the light is crucial for maximizing the lifetime of our dark polaritons. In particular, while probing the system, we use a 5 G bias magnetic field directed along the Rydberg coupling beam propagation axis in order to provide a Zeeman splitting within each of the atomic state manifolds (Fig. S4c). The sample is also repeatedly optically pumped along that same axis to ensure that all atoms start in the $|F = 2, m_F = -2\rangle$ state. Because the Rydberg coupling beam is coaligned with the magnetic field, and the science cavity mode axis is only $\sim 30^\circ$ away, the circularly polarized cavity photons only couple the atoms to a single spin state in each manifold. These conditions make our polarized atoms behave much more like a three-level system than an unpolarized sample; the three relevant levels are

$|5S_{1/2}, F = 2, m_F = -2\rangle$, $|5P_{3/2}, F = 3, m_F = -3\rangle$, and $|111D_{5/2}, m_J = 5/2\rangle$ where we note that the hyperfine splitting of the Rydberg state is negligible. We have found that this setup maximizes the dark polariton lifetime and minimizes the creation of stray Rydberg atoms. For more details on the experiment setup, see SI A 5.

The full experiment procedure is depicted in Fig. S4a. Because we are able to trap the atoms while probing, we now spend approximately 200 ms preparing the sample and 100 ms performing science measurements in each trial, for a duty cycle of roughly 33%; this represents a dramatic improvement over the previous scheme, in which the duty cycle was approximately 1% [17, 18]. Note that the time spent loading the magneto-optical trap is also used by the computer to prepare the control electronics for running the next iteration of the experiment sequence.

We have also made a number of technical improvements to the Floquet setup relative to our original implementation in Ref. [18]. In this work the laser beam inducing the sinusoidally modulated AC Stark shift of the $5P_{3/2}$ state (the ‘Floquet beam’) has a wavelength of $\lambda_f = 1529$ nm near the $5P_{3/2} \rightarrow 4D_{3/2}$ and $5P_{3/2} \rightarrow 4D_{5/2}$ transitions. This new Floquet beam has a much greater detuning from the $5S_{1/2} \rightarrow 5P_{3/2}$ at 780 nm than the old Floquet beam at 776 nm, which was used in our previous work. This increased detuning dramatically reduces the inhomogeneous broadening of the atomic ground state caused by the inhomogeneous intensity of the Floquet beam, thereby maximizing the coherence time of the dark polaritons. We set the frequency components of the multichromatic Floquet field and their relative amplitudes in order to sinusoidally modulate the energy of the $5P_{3/2}$ state while keeping its average energy constant [18]. In particular, the Floquet laser is locked at a frequency 7 GHz detuned from the $5P_{3/2} \rightarrow 4D_{5/2}$ transition, such that it has nearly equal and opposite detunings from $4D_{5/2}$ and $4D_{3/2}$ which are split by 13.5 GHz. After amplifying the beam with an erbium-doped fiber amplifier we use a fiber electro-optic modulator (EOM) to simultaneously phase-modulate the light at frequencies of 8.500 GHz and 8.573 GHz; each of the resulting first order EOM-induced sidebands has a power approximately 1/6 that of the optical carrier. We fine-tune the strength of the sidebands in order to achieve a large modulation amplitude of the $5P_{3/2}$ energy at $f_{\text{mod}} = 73$ MHz while its average energy is unchanged.

6. Cavity details

This experiment utilizes two crossed nonplanar cavities; a primary ‘science’ cavity for 780 nm photons and a build-up cavity for 480 nm photons. It is necessary to use a separate build-up cavity because the 480 nm control field needs to cover an area larger than that spanned by

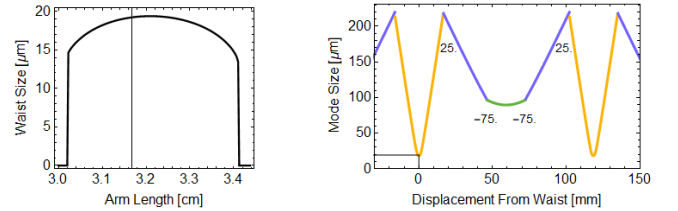


FIG. S5. **Science Cavity Mode Size.** (left) The waist size of the cavity is plotted as the total length of the cavity is scaled in proportion to the lower arm length. The nearly three-fold degenerate point we operate at is shown by the vertical line. (right) A plot of the mode size as a function of the distance along the optical axis throughout the cavity, including the small primary 19 μm waist in the lower arm (orange), where the atoms are placed, along with a larger 90 μm waist in the upper arm (green). The four cavity mirrors are labelled between the arms of the cavity with their radius-of-curvature in mm. The mode size is periodic in the cavity length, which is approximately 120 mm.

the 780 nm modes used in any experiment. To maintain sufficient control field Rabi coupling over the first five degenerate modes would then require ~ 10 W of power in single pass. As this is significantly beyond maximum available laser power, we introduced a build-up cavity for the Rydberg control field. This cavity is nonplanar to ensure circularly polarized modes, maximizing the Rabi coupling; it must also be a running wave cavity to avoid having nodes of the Rydberg coupling field inside the atom cloud.

To reduce noise and promote stability, both cavities’ mirrors and piezos are mounted in a monolithic nonmagnetic steel structure. The science cavity is a 4 mirror, 3-fold degenerate nonplanar cavity modeled off of our previous work using such cavities without cold atoms present [19, 56]. There were two primary design challenges in making these nonplanar cavities compatible with the atomic physics setup. First we needed a smaller waist size than we had previously achieved with our degenerate nonplanar cavities, since this cavity needed to be compatible with Rydberg mediated photon-photon interactions. This is a particular challenge because we also require Laguerre-Gaussian eigenmodes, and the standard techniques for reducing the waist such as reducing the radius-of-curvature of the cavity mirrors increases astigmatism, which then favors Hermite-Gaussian modes. While we previously explored single and two mode blockade physics in a planar cavity with a 14 μm waist [17, 18], we relaxed the waist size requirement to ~ 20 μm and increased the target Rydberg level accordingly. This target was then achievable by using convex, -75 mm radius-of-curvature mirrors in the upper arm along with standard 25 mm radius-of-curvature mirrors in the lower arm Fig. S5.

The second design challenge for this cavity concerned reaching threefold degeneracy with the cavity in vacuum.

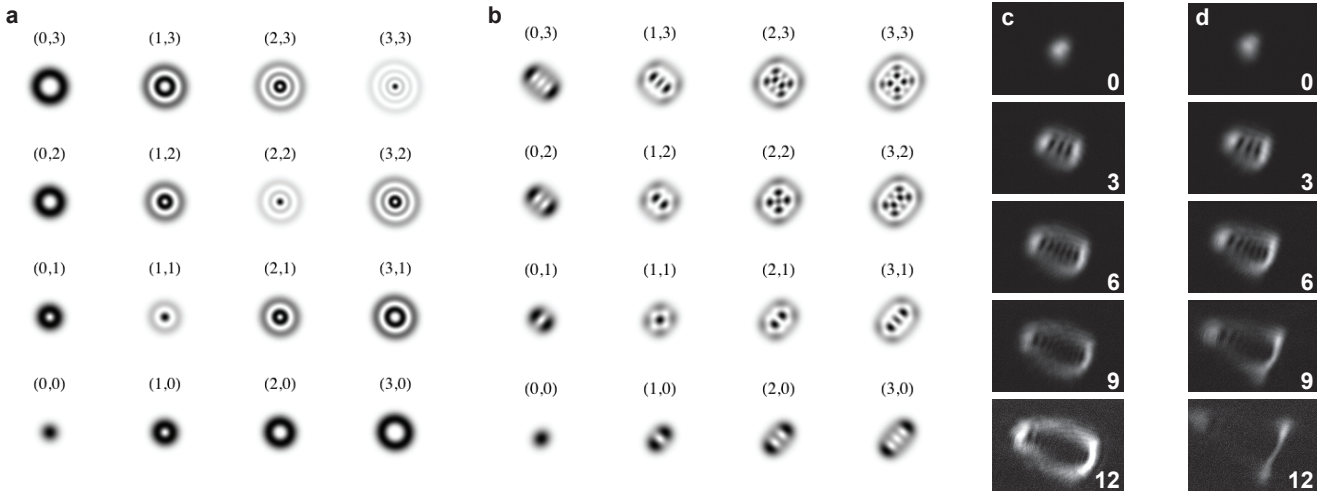


FIG. S6. Comparison of Mode Profiles. **a**, The cavity modes are expected to be near-perfect Laguerre Gaussian modes at the lower waist. **b**, Significant astigmatism causes the cavity modes at the upper waist to have significant Hermite Gaussian character. **c**, Away from degeneracy (30 MHz splitting between modes), the science cavity's eigenmodes are as expected; however **d**, as we approach degeneracy (13 MHz splitting) the modes couple significantly, as is evident from the strong threefold symmetry that develops. The modes also become lossy, indicating that the coupling is from long range aberration rather than local disorder.

Prior degenerate cavities were mounted in two halves separated by a micrometer stage. Adjusting this stage brought the modes into degeneracy. Since this technique is incompatible with vacuum, and the bake-out of the chamber was likely to change the cavity alignment slightly, we introduced a slow long throw piezo behind one of the cavity mirrors, providing a $63\ \mu\text{m}$ free stroke, corresponding to an approximately 6% change in the transverse mode spacing. Thus after aligning and gluing the cavity outside the vacuum chamber (and taking into account the index of refraction of air) and then baking out the chamber, degeneracy was within range of the long throw piezo.

Otherwise, this cavity is fairly standard. The two convex mirrors are coated to outcouple light, with 99.91(1)% reflection, while the lower mirrors are HR coated, so that there are effectively only two ports in this cavity. Similar coatings at 1560 nm provide for convenient cavity length stabilization, enabled by a short-throw ring piezo stack actuating a cavity mirror. After construction and installation, we achieve a finesse of 1900(50) with a free spectral range of 2500(1) MHz at our operating point near, but not at, mode-degeneracy.

The presence of significant astigmatism causes several issues in this cavity. First it makes the expected eigenmodes not Laguerre Gaussian in the upper waist. These modes are intermediate between Laguerre Gaussian and Hermite Gaussian and are connected to pure Laguerre Gaussian modes through an astigmatic mode converter [80]. This does not affect the physics at the lower waist, at which the cavity modes are nearly-pure Laguerre Gaussian modes (see SI A 7). Since we inject

light into the cavity through the upper mirrors, we select the desired mode by programming the corresponding upper waist profile onto a digital micromirror device [78]. Cubic aberrations associated with the astigmatism induces coupling between modes of our degenerate manifold, causing distortion and dramatically increased loss near degeneracy. Although the long throw piezo can move the cavity into degeneracy for every third mode in order to form a Landau level for cavity photons, the mode-repulsion and increased loss caused by cubic astigmatism makes this useless (see Fig. S8). Thus we operate with Landau level modes split out by around 70 MHz (using both the long throw piezo and a heating wire), and make up the energy-difference with Floquet modulation as discussed in Methods D.

Relative alignment between the two cavities is critical. Since the alignment was performed outside of vacuum before bakeout, we anticipated significant drift between the cavity modes. As such, we aimed to produce a very large waisted build-up cavity ($\sim 320\ \mu\text{m}$), with a corresponding increase in desired finesse. The increased mode area along with a desire for significantly higher blue Rabi frequency (to open up the possibility of increasing the atomic density) led to a mirror coating order specifying 99.97% reflectors for a finesse 10,000 cavity. In fact, the mirrors we received were 99.985% *loss dominated* reflectors. This higher than expected loss at 480 nm made these mirrors useless for the build-up cavity. Rather than wait the several months required to replace these mirrors, we instead used readily available mirrors with 1.5 m radius-of-curvature and a reflectivity of 97% at 480 nm. Rebuilding the cavity to include one of these mirrors pro-

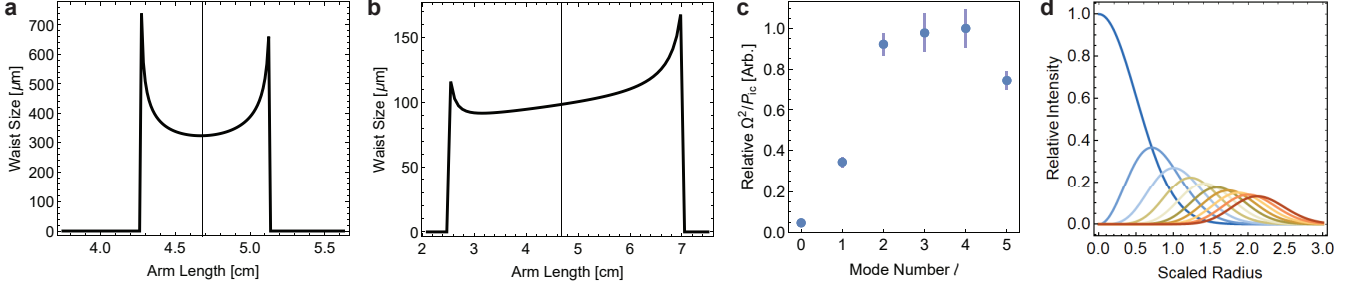


FIG. S7. Buildup Cavity Modes and Relative Alignment. **a**, The originally intended build-up cavity mode size was more than three times larger than ,**b**, the mode size of the cavity after rebuilding to include the new high transmitter. **c**, We fit the measured control Rabi frequency from cavity Rydberg EIT transmission at 40S and plot the ratio of that frequency to the intracavity circulating power versus the LG mode injected into the build-up cavity, finding a uniform factor of ~ 20 improvement for $l = 2, 3$, or 4 compared to $l = 0$. **d**, This approximately uniform improvement indicates a relative shift between the mode centers of the two cavities by around 1.4 build-up cavity waists ($140 \mu\text{m}$). Each curve shows the radial intensity profile of a Laguerre-Gauss mode.

duced a finesse 190 single ended cavity with a waist size of $98 \mu\text{m}$ at the location of the atoms, providing enough intensity build-up to achieve a sufficient control Rabi frequency over the first few degenerate modes of the science cavity.

Before bakeout, proper alignment between the two cavities was ensured by moving a thin wire cross on a translation stage and seeing both cavity modes spoil simultaneously. After installation and bakeout, there remained significant concern about the relative alignment between the cavity modes. Initial EIT signals showed a very weak control Rabi frequency. Coupling into higher order LG modes of the build-up cavity resulted in a much greater control Rabi frequency, normalized to the intracavity circulating power (See Fig. S7c). Comparison with the relative intensities of the various higher order LG modes as a function of radius (Fig. S7d) indicates that the improvement in overlap between the higher order build-up cavity modes and the science cavity mode arose from an $\sim 140 \mu\text{m}$ shift.

In order to drive a higher order LG mode, we convert a large Gaussian beam into an $\text{LG}_{2,0}$ via a vortex half-wave retarder with $> 80\%$ efficiency. This, combined with the significant $\sim 80\%$ peak intensity reduction still leaves a factor of 5 build-up in the circulating power.

7. Modes in the Lower Resonator Waist

As stated in SI A 6, the resonator modes at the location of the atomic sample *should* form the Lowest Landau level on the surface of a cone [19]. For our case of a cone corresponding to $1/3$ of the plane with no magnetic flux threading its tip, these modes are, in the symmetric gauge, $\psi_{L=3l}(z) = \sqrt{\frac{1}{\pi L! l_B^2}} \left(\frac{z}{l_B}\right)^L e^{-z\bar{z}/2l_B^2}$, where $z \equiv x + iy$, and l_B is the harmonic oscillator length of the lowest Landau level.

Taking the modes of the lower-waist of the resonator ψ_L^{actual} , as plotted in the previous section SI A 6, and overlapping them with the ψ_L as written above, provides near-unity overlap once a local gauge transformation $\psi \rightarrow \psi \times e^{i\chi}$, for $\chi \equiv (\frac{x}{36\mu\text{m}})^2 + (\frac{y}{36\mu\text{m}})^2 + 2\frac{xy}{(59\mu\text{m})^2}$ is applied:

For a waist $w_{cav} = \sqrt{2}l_B \approx 19.2\mu\text{m}$, we find a numerical overlap-squared between the L^{th} gauge-adjusted Laguerre-Gauss mode and the L^{th} cavity mode of $F_L \equiv |\langle \psi_L^{actual} | e^{i\chi} | \psi_L \rangle|^2 \approx 0.99985 - \left(\frac{L}{117}\right)^2$; that is, $F_L > 0.993$ for $L \leq 9$ – the resonator modes that we are employing are expected to be almost perfectly Laguerre-Gaussian.

It bears mentioning that the local gauge transformation $e^{-i\chi}$ is pure-phase (as all such gauge transformations are), and since it is the same for all resonator modes, it does not impact the collisional matrix elements, and hence does not impact the intra-cavity physics. It does weakly perturb the propagation of the light outside of the resonator, which is why (in conjunction with the subsequent astigmatism imposed on the light as it exits the resonator), we reference our Laughlin states back to a virtual image plane at the resonator mode waist. *Such aberrations could be simplified corrected using a combination of spherical/cylindrical lenses outside of the cavity and free-space propagation.*

8. Electric field management

Special care was taken to engineer the electric field environment experienced by the Rydberg atoms. Most importantly, all surfaces, either metal or dielectric are kept at least 10 mm from the atoms, and line-of-sight between the atoms and dielectric surfaces is minimized to just the lower cavity mirrors. Piezos are shielded by grounded metal and are driven so that their surfaces that

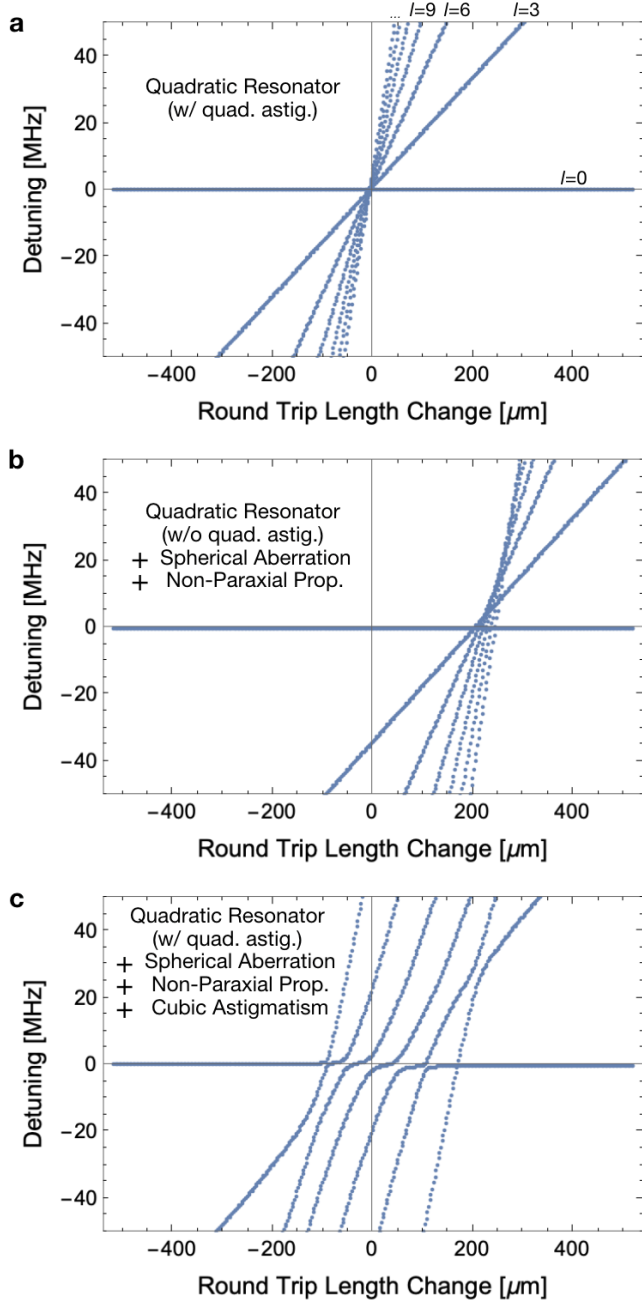


FIG. S8. Impact of Higher-Order Aberrations on the Resonator Mode-Structure. Within the quadratic optic/paraxial propagation approximation **a**, the modes (labeled for $l=0,3,6,9$) of the conical lowest Landau level of our twisted cavity are uniformly spaced in energy, and reach true degeneracy at a particular cavity length, as shown by ABCD-matrix numerics. When all astigmatism is removed, but spherical aberration and non-paraxial propagation are added to the model **b**, the modes no longer reach true degeneracy, but do not mix, because they are spaced by three cavity-mode quanta (nodes for a planar cavity, and units of angular momentum for a twisted cavity), and as such quartic disorder cannot couple them. When the quadratic and cubic aberrations due to off-axis incidence are further added to the model **c**, large avoided crossings appear.

face the atoms are held at ground. In order to cancel the remaining background electric field \mathbf{E}_{bkg} experienced by the atoms, the structure also supports eight electrodes which can apply additional electric fields and gradients at the location of the atomic cloud. The cavity structure itself is electrically isolated and controlled, acting as a ninth electrode. Typical scans of the dark polariton spectrum as a function of this applied electric field \mathbf{E} are shown in Fig. S9. These scans enable us to identify the applied field which is necessary to achieve a net electric field $\mathbf{E}_{\text{net}} = \mathbf{E}_{\text{bkg}} + \mathbf{E} = 0$ at the location of the atoms.

We observed drift of the electric field which we attribute to Rb (or Rb ion) accumulation on the cavity structure and mirrors. We mitigate this issue by pulsing a ~ 100 mW UV flashlight centered around 365 nm while jumping the set voltage of the entire cavity structure to $+10$ V while the MOT is loading (Fig. S10). These passive mitigating factors along with active electric field control work in concert to enable our experiments with the $111D_{5/2}$ Rydberg state with negligible broadening due to electric field inhomogeneity and hours-long stability. In particular, over time we observe irregular electric field drift which is typically smaller than 0.05 (V/m)/h. Moreover, based on the broadening of the $l = 6$ dark polariton feature at finite electric field offsets, we estimate that the field varies by less than 0.1 V/m across the 100 micron diameter of that mode. Based on the electric polarizability of $6 \text{ MHz}/(\text{V/m})^2$ for the $111D_{5/2} m_J = 5/2$ state, the inhomogeneous broadening of the dark polaritons as well as the drift of their energy over two hours should both be less than 60 kHz, which is comparable to or below the linewidth of the dark polaritons that we typically work with.

Supplement B: Theory

1. Collective atomic excitations

Even though thousands of atoms are present in the cavity, only a small subset of the possible atomic excitations are coupled to the cavity photons. In fact, each cavity mode couples to a unique collective $5P_{3/2}$ excitation, which is subsequently coupled by the Rydberg control laser to a unique collective Rydberg excitation (see Fig. Extended Data 3b). These collective excitations are superposition states in which one excitation is shared by many atoms with a spatial waveform that is proportional to the field of the corresponding cavity mode. In particular, photons in the cavity mode with angular momentum l (created by the operator a_l^\dagger) couple to the collective $5P_{3/2}$ excitation created by the operator,

$$p_l^\dagger = \frac{1}{g_l} \sum_{m=1}^{N_{at}} g_{ml} \sigma_m^{eg},$$

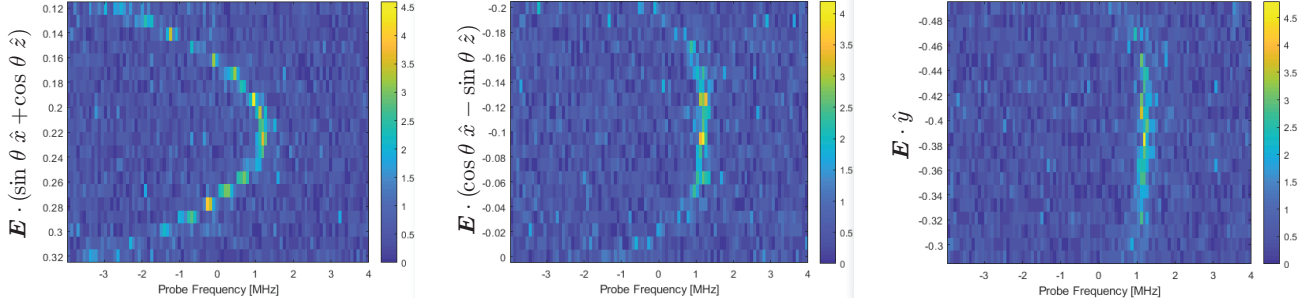


FIG. S9. Electric Field Scans. The transmission rate (colorbar) for Rydberg-like dark polaritons is plotted versus probe frequency and applied electric field (units of V/dm). We scan the electric field \mathbf{E} along three axes, as indicated on the individual plots, which are rotated around \hat{y} from the typical coordinate axes used in this work by the angle $\theta \approx 30^\circ$. To maintain an optically pumped sample, we apply a 5 G magnetic field along the blue cavity axis, which results in the large sensitivity in the leftmost plot, while suppressing the electric polarizability along the orthogonal axes observed in the other two plots. Strong orthogonal electric fields break the m_j splitting along the magnetic field axis, cause coupling to many Rydberg states, and dramatically broaden and shrink the dark polariton resonance.

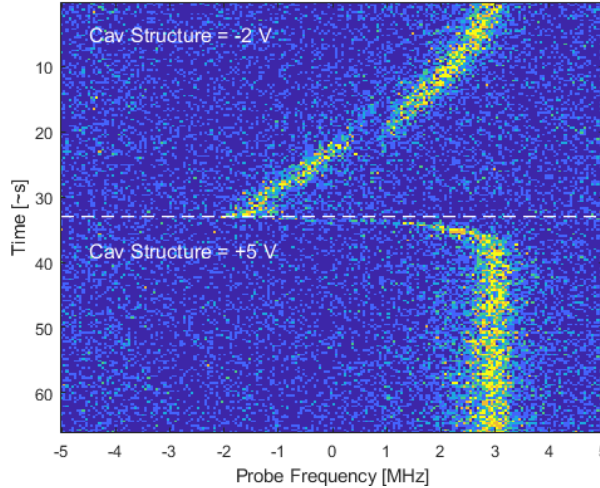


FIG. S10. Stray Charge Mitigation. The transmission spectrum near the dark polariton resonance over time; blue indicates low transmission, yellow indicates high transmission. Illumination of the cavity structure with UV light can change the build up of stray charges that cause electric field drift and thus the drift of the dark polariton resonance. Furthermore, the simultaneous application of a voltage on the cavity structure dramatically changes the behavior of mobile charges. A substantial negative voltage appears to increase the drift rate of the electric field (above the white dashed line), while the application of a substantial positive voltage causes the field to rapidly equilibrate and strongly suppresses further drift; this suppression stabilizes the dark polariton resonance and provides the best conditions for our experiments (below the white dashed line).

where $g_l^2 \equiv \sum_{m=1}^{N_{at}} |g_{ml}|^2$ is the total atom-photon coupling strength for that mode and the coupling of cavity photons to the m 'th atom $g_{ml} = g_{\text{sing}} \phi_l(\mathbf{x}_m)/\phi_0(0)$ is proportional to the electric field ϕ_l (normalized such that $\int d^2\mathbf{x} |\phi_l(\mathbf{x})|^2 = 1$) at the position \mathbf{x}_m of the atom

as well as the peak single-atom coupling strength g_{sing} . The operator σ_m^{eg} excites atom m from the ground state to the $5P_{3/2}$ state. Similarly, the corresponding collective Rydberg excitation is created by the operator,

$$r_l^\dagger = \frac{1}{g_l} \sum_{m=1}^{N_{at}} g_{ml} \sigma_m^{rg},$$

where the operator σ_m^{rg} excites atom m from the ground state to the Rydberg state. Because the orthonormal set of cavity modes couples one-to-one with the orthonormal set of collective atomic excitations, the atom-cavity coupling does not directly mix the cavity modes together. Therefore, only the Rydberg-Rydberg interactions cause photons to move between the modes. For more on the orthogonality of the collective excitations see SI B2 of Ref. [18].

2. Floquet polaritons are protected from intracavity aberrations

It is often technically challenging to form a degenerate manifold of cavity modes, because mirror defects and intracavity aberrations such as astigmatism can induce couplings between the modes which break their degeneracy. Our Floquet scheme makes it possible to form an effectively degenerate manifold of dark polaritons, in which the polaritons have the same quasi-energy, without making the bare cavity modes degenerate. Naïvely, it might seem that the Floquet polaritons should inherit all of the couplings from their Rydberg and cavity photonic parts, in which case the degeneracy would still be split by the intracavity aberrations. However, as we will demonstrate below, the aberration couplings between Floquet polaritons are strongly suppressed, precisely because the

large energy separation between the bare cavity modes remains.

We next demonstrate these features more formally. The behavior of Floquet polaritons is best understood in the high frequency approximation [81], as detailed in Ref. [18]. We begin with the time-dependent Hamiltonian of the system,

$$\begin{aligned} H(t) = & \sum_n^{N_{cav}} \left(\delta_c^n a_n^\dagger a_n + \bar{\delta}_e p_n^\dagger p_n + \delta_2 r_n^\dagger r_n \right. \\ & + \sum_{m=-\infty}^{\infty} g_m^n e^{im\omega t} p_n a_n^\dagger + h.c. + \\ & + \sum_{m=-\infty}^{\infty} \Omega_{-m} e^{-im\omega t} r_n p_n^\dagger + h.c. \Big) \\ & + \frac{1}{2} \sum_{nmpq}^{N_{cav}} U_{nmpq} r_n^\dagger r_m^\dagger r_p r_q \\ & + \sum_{n,q \neq n}^{N_{cav}} D_{nq} a_n^\dagger a_q e^{i(k_q - k_n)\omega t} + h.c. \end{aligned}$$

The first line accounts for the relative energies of the $N_{cav} = 3$ cavity modes, with energy δ_c^n for the n 'th cavity mode with annihilation operator a_n , time-averaged energy $\bar{\delta}_e$ of the collective $5P_{3/2}$ states with annihilation operator p_n , and energy δ_2 for the collective Rydberg states with annihilation operator r_n . The next line denotes the atom-cavity coupling g_m^n in mode n through Floquet band m ; $\omega = 2\pi f_{\text{mod}}$ is the modulation angular frequency. The third line denotes the Rydberg couplings Ω_m via Floquet band m . The fourth line accounts for the Rydberg-Rydberg interactions with strength U_{nmpq} between all possible combinations of modes. The final line represents intracavity aberrations, which couple between cavity modes n and q with strength D_{nq} .

The experimentally relevant case is the limit in which each cavity mode n is near-detuned to a band k_n of the $5P_{3/2}$ state and the Rydberg coupling laser is also near resonant for driving $5P_{3/2} \rightarrow 111D_{5/2}$ via band l . Under these conditions, we can write $\delta_c^n \equiv k_n \omega + \epsilon_c^n$, $\bar{\delta}_e \equiv \epsilon_p$, $\delta_2 = l\omega + \epsilon_r$, such that the quasienegies satisfy,

$$\epsilon_c, \epsilon_p, \epsilon_r \ll \omega.$$

Transforming to the frame of this resonant coupling,

$$\begin{aligned} a_n &\rightarrow e^{ik_n\omega t} a_n, \\ r_n &\rightarrow e^{il\omega t} r_n, \end{aligned}$$

the Hamiltonian becomes,

$$\begin{aligned} H(t) = & \sum_n^{N_{cav}} \left(\epsilon_c^n a_n^\dagger a_n + \epsilon_p p_n^\dagger p_n + \epsilon_r r_n^\dagger r_n \right. \\ & + \sum_{m=-\infty}^{\infty} g_m^n e^{im\omega t} p_n a_n^\dagger + h.c. + \\ & + \sum_{m=-\infty}^{\infty} \Omega_{-m} e^{-im\omega t} r_n p_n^\dagger + h.c. \Big) \\ & + \frac{1}{2} \sum_{nmpq}^{N_{cav}} U_{nmpq} r_n^\dagger r_m^\dagger r_p r_q \\ & + \sum_{n,q \neq n}^{N_{cav}} D_{nq} a_n^\dagger a_q e^{i(k_q - k_n)\omega t} + h.c. \end{aligned}$$

Since we have now transformed to this basis where the quasienegies are all similar, the dynamics of the system will be dominated by the coupling terms which are not rotating.

Two features of this Hamiltonian are worthy of particular attention. First, because all of the bare Rydberg states are degenerate, and therefore couple to the P-state through the same Floquet band, all of the Rydberg-Rydberg interaction terms remain resonant (not rotating) even after this transformation. In contrast, because the bare cavity modes were not degenerate, and each couples to the P-state through a different Floquet band, the aberration couplings between the cavity mode now have a rapidly rotating complex phase, indicating that they are off-resonant.

At lowest order in the high frequency approximation, which is equivalent to the rotating wave approximation at this order, the effective Hamiltonian is just the average of the full, time-dependent Hamiltonian above,

$$H_F^{(1)} = H_0,$$

where H_m is the m 'th Fourier component of the Hamiltonian,

$$H_m = \frac{1}{T} \int_0^T e^{-im\omega t} \tilde{H}(t) = H_{-m}^\dagger$$

$$\begin{aligned} H_F^{(1)} = & \sum_n^{N_{cav}} \left(\epsilon_c^n a_n^\dagger a_n + \epsilon_p p_n^\dagger p_n + \epsilon_r r_n^\dagger r_n \right. \\ & + g_m^n p_n a_n^\dagger + \Omega_{-l} r_n p_n^\dagger + h.c. \Big) \end{aligned} \quad (\text{S1})$$

$$\begin{aligned} & + \frac{1}{2} \sum_{nmpq}^{N_{cav}} U_{nmpq} r_n^\dagger r_m^\dagger r_p r_q \Big) \\ & + \sum_{n,q \neq n}^{N_{cav}} D_{nq} \delta_{k_q, k_n} a_n^\dagger a_q \end{aligned} \quad (\text{S2})$$

As expected, at this level of approximation, mirror disorder is only relevant if the bare cavity modes are degenerate, as determined by the Kronecker delta δ_{k_q, k_n} in the final line which requires that the modes couple to the P-state through the same Floquet band. The Rydberg interactions all contribute fully at the usual level because the bare Rydberg states in the absence of modulation were already degenerate.

At next order we see the effects of mirror disorder between cavity modes which are not naively degenerate. The next order contribution to the effective Hamiltonian is,

$$H_F^{(2)} = \sum_{m \neq 0} \frac{H_m H_{-m}}{m \hbar \omega},$$

where the relevant Fourier components are,

$$\begin{aligned} H_m = & \sum_n^{N_{cav}} \left(g_{-m+k_n}^n p_n^\dagger a_n + g_{m+k_n}^n p_n a_n^\dagger \right. \\ & \left. + \Omega_{-m-l} r_n^\dagger p_n + \Omega_{m-l} r_n p_n^\dagger \right) \\ & + \sum_{n,q \neq n}^{N_{cav}} D_{nq} a_n^\dagger a_q \delta_{m,k_q-k_n} + D_{nq} a_n a_q^\dagger \delta_{-m,k_q-k_n}. \end{aligned}$$

At this order, the effective Hamiltonian gains a variety of terms with strengths D^2/ω , Dg/ω , or $D\Omega/\omega$. As long as all of the coupling strengths $g, \Omega, D \ll \omega$ are small compared to the modulation frequency, these terms will be negligible. Overall, this treatment demonstrates how the Floquet scheme enables us to create degenerate manifolds of dark polaritons while strongly suppressing the broadening that intracavity aberrations would cause in a degenerate manifold of bare cavity modes.

3. Many-body spectrum

The many-body spectrum for two excitations in the three modes accessible in this paper (Fig. 3b of the main text) is calculated as follows. When the three modes have been made degenerate with energy per particle E_{pol} , the energies of multi-particle states are only differentiated by the interaction Hamiltonian,

$$H_{int} = \frac{U}{2} \int d^2 z \psi^\dagger(z) \psi^\dagger(z) \psi(z) \psi(z), \quad (S3)$$

where $\psi(z)$ is the field operator and we have made the approximation of contact interactions with strength U . The approximation of contact interactions is best justified when the Rydberg blockade radius is small compared to the cavity mode waist. However, even when the blockade radius and mode waist are comparable, the

spectrum remains qualitatively similar. Note that the interaction strength U typically has a large imaginary component [74], but we depicted a larger real than imaginary component in Fig. 3a & b to make the visualization clear.

Projecting the interaction Hamiltonian into the basis of our degenerate Landau level yields,

$$H_{int} = \frac{U}{2} \sum_{ijkl \in \{3,6,9\}} \beta_{ijkl} a_i^\dagger a_j^\dagger a_k a_l, \quad (S4)$$

where the interaction energies among modes are determined by the overlap integrals,

$$\beta_{ijkl} = \int d^2 z \phi_i^*(z) \phi_j^*(z) \phi_k(z) \phi_l(z), \quad (S5)$$

and the wavefunction for the mode with angular momentum $\hbar l$ is,

$$\phi_l(z) = \frac{1}{\sqrt{2^{l+1} l! \pi}} z^l e^{-|z|^2/4}. \quad (S6)$$

Diagonalizing this interaction Hamiltonian within the two-particle manifold yields the energy spectrum of two-particle states in our system, including the Laughlin state with zero interaction energy.

4. Varieties of Two-Particle Laughlin States

Two photons in any three evenly spaced angular momentum modes can form a Laughlin state. While these Laughlin states differ in the exact form of their wavefunctions, they all enable the two particles to minimize their interaction energy while remaining in the lowest Landau level. The two particle Laughlin states in which we are interested can be expressed in real space as,

$$\psi_L(z_1, z_2; m, n) = N_{mn} z_1^m z_2^m (z_1^n - z_2^n)^2 e^{-(|z_1|^2 + |z_2|^2)/4}, \quad (S7)$$

where $z_j \equiv x_j + iy_j$ represents the position of particle j in units of the magnetic length, m & n are positive integers, and N_{mn} is an overall normalization factor ensuring $\int \int d^2 z_1 d^2 z_2 |\psi_L|^2 = 1$. Note that these states all share the property that particles avoid each other, since $\psi_L(z_1 = z_2; m, n) = 0$.

The two particle Laughlin states $\psi_L(z_1, z_2; m, n)$ can be composed from the three angular momentum modes with $l = m$, $m+n$, and $m+2n$. To explicitly perform the transformation to the angular momentum basis we can expand the polynomial pre-factor, yielding,

$$\begin{aligned} \psi_L(z_1, z_2; m, n) = & N_{mn} e^{-(|z_1|^2 + |z_2|^2)/4} \\ & \times (z_1^m z_2^{m+2n} + z_1^{m+2n} z_2^m - 2z_1^{m+n} z_2^{m+n}). \end{aligned} \quad (S8)$$

Comparing this form to the single particle angular momentum modes,

$$\phi_l(z) = \frac{1}{\sqrt{2^l l!}} z^l e^{-|z|^2/4}, \quad (\text{S9})$$

reveals that the first two terms on the right-hand side of Eq. S8 correspond to the properly symmetrized two-particle angular momentum state ϕ_{l_1, l_2} for particles with angular momenta $l_1 = m$ and $l_2 = m + 2n$. The last term on the right-hand side of Eq. S8 corresponds to $\phi_{m+n, m+n}$. Accounting for normalization factors of each angular momentum state, we obtain,

$$\begin{aligned} \psi_L(z_1, z_2; m, n) &= N_{mn} e^{-(|z_1|^2 + |z_2|^2)/4} \\ &\times (\sqrt{2} \sqrt{2^{2n+m}(2n+m)!} \sqrt{2^m(m)!} \phi_{2n+m, m}(z_1, z_2) \\ &- 2^{n+m+1} (n+m)! \phi_{n+m, n+m}(z_1, z_2)), \end{aligned} \quad (\text{S10})$$

or approximately in the notation of the main text (where $|uv\rangle \equiv |u, v\rangle$ means a two-particle state with the individual particles possessing angular momenta $u\hbar$ and $v\hbar$ about the origin),

$$\begin{aligned} |L\rangle_{mn} &= \\ N_{mn} &(\sqrt{2} \sqrt{2^{2n+m}(2n+m)!} \sqrt{2^m(m)!} |m, m+2n\rangle \\ &- 2^{n+m+1} (n+m)! |m+n, m+n\rangle). \end{aligned} \quad (\text{S11})$$

Therefore, in each Laughlin state, the ratio α_{mn} between the populations in $|m, m+2n\rangle$ and $|m+n, m+n\rangle$ is,

$$\alpha_{mn} = \frac{(2n+m)!m!}{2(n+m)!^2}. \quad (\text{S12})$$

For the Laughlin state with $m = n = 3$ used in this work, we find $\alpha_{mn} = \frac{21}{10} = 2.1$, as reported in the main text. Note that, for each Laughlin state $|L\rangle_{mn}$, there is a corresponding “anti-Laughlin” state,

$$\begin{aligned} |AL\rangle_{mn} &= \\ N_{mn} &(2^{n+m+1} (n+m)! |m, m+2n\rangle \\ &+ \sqrt{2} \sqrt{2^{2n+m}(2n+m)!} \sqrt{2^m(m)!} |m+n, m+n\rangle), \end{aligned} \quad (\text{S13})$$

which exhibits spatial bunching instead of anti-bunching.

Physically, one can think of the choice of n as splitting the ordinary Landau level (containing every angular momentum mode $l = 0, 1, 2, \dots$) into n separate Landau levels existing on cones with a spatial curvature of $R(x, y) = 4\pi(1 - \frac{1}{n})\delta^{(2)}(x, y)$ localized at the cone tip, where $\delta^{(2)}(x, y)$ is the two-dimensional Dirac delta function [19, 56, 82]. The n cones with the same curvature correspond to different choices of the lowest angular momentum mode m , which determines the effective magnetic flux $\frac{m \bmod n}{n}\Phi_0$ threaded through the cone tip, where Φ_0 is the magnetic flux quantum. Moreover, when

m exceeds n , the Laughlin state has $\text{Floor}(m/n)$ quasi-holes pinned at the origin, where $\text{Floor}(x)$ denotes the largest integer less than or equal to x .

Interestingly, the azimuthal correlations $g_{mn}^{(2)}(\phi) \propto |\psi_L(z_1 = z_2 e^{i\phi}; m, n)|^2$ are independent of m and have a very simple dependence on n . Using the form of the wavefunction in Eq. S7, it is straightforward to find that,

$$g^{(2)}(\phi)_{mn} \propto \sin^4\left(\frac{n}{2}\phi\right). \quad (\text{S14})$$

Moreover, when viewed in terms of the angle $\phi_{\text{cone}} = n\phi$ around the cone tip, the azimuthal correlation function is entirely independent of m and n .

Since these Laughlin states are all closely related physically, our choice of $m = n = 3$ was made for technical reasons. First, we chose to make only every third angular momentum state degenerate to protect the Landau level from intracavity astigmatism (see Ref. [19]). In the end, because we use Floquet polaritons, this choice was likely not necessary (see SI B 2); however, the length of our cavity is not sufficiently tunable to bring any other set of angular momentum modes near enough to degeneracy to be convenient for our Floquet scheme. Second, we choose $m = 3$, making $l = 3$ our lowest angular momentum mode rather than $l = 0$, because it yields $\alpha_{33} = 2.1$ much smaller than $\alpha_{03} = 10$. Smaller α_{mn} increases the contribution of $|m+n, m+n\rangle$ to the Laughlin state, improving the coupling of our coherent probe on $l = m+n$ to the Laughlin state relative to the anti-Laughlin state.

5. Collision analysis

We compare our collision experiments in Fig. 2c of the main text with numerical calculations using multimode non-Hermitian perturbation theory (NHPT; see SI B9 of Ref. [18] for details). NHPT enables us to perform a brute force calculation including the relevant microscopic degrees of freedom for a simulated random sample of atoms coupled to our multimode cavity with up to two excitations (photons or atomic excitations) present in the system. Our NHPT calculation does not explicitly include the Floquet scheme; therefore, we choose settings for the static calculation which best approximate the conditions arising from the Floquet scheme. In particular, the solid curve in Fig. 2c is calculated with cavity mode detunings of $\delta c_3 = -2\pi \times 2$ MHz, $\delta c_6 = 0$, and $\delta c_9 = 2\pi \times 2.5$ MHz to approximate the effects of the different intermediate state detunings for the three angular momentum modes revealed in Fig. Extended Data 4. As a result, when the simulations are performed with zero energy mismatch $E_3 + E_9 = 2E_6$, unlike the experiments the simulations do *not* satisfy the condition $E_3 = E_9 = E_6$ that all of the single dark polariton states have the same energy. Since the collision physics should be dominated by the energies of

the two polariton states, we believe that this approach still captures the relevant physical parameters of the system. In addition to those cavity detunings, the simulations are performed with the van der Waals interaction strength coefficient $C_6 = -2\pi \times 1.5 \times 10^8 \text{ MHz}\cdot\mu\text{m}^6$ approximately corresponding to the $111\text{D}_{5/2}$ Rydberg state, an overall intermediate state detuning of $2\pi \times 0.5 \text{ MHz}$, total atom-photon coupling strengths in each mode of $g_3 = g_9 = 2\pi \times 4.5 \text{ MHz}$ and $g_6 = 2\pi \times 11.9 \text{ MHz}$, Rydberg coupling strength $\Omega = 2\pi \times 2.2 \text{ MHz}$ for each atom, and effective Rydberg decay rate $\gamma_R = 2\pi \times 50 \text{ kHz}$. As in the actual experiments, we numerically scan the energy mismatch by varying the two-photon detuning or equivalently the energy of the Rydberg state. After performing the NHPT calculation with these parameters, we use a single parameter least squares fit to adjust the vertical scale of the NHPT result based on the observed count rates in Fig. 2c.

The collision rates observed in Fig. 2c of the main text are well captured by the numerical calculation. In particular, to perform a detailed comparison, we fit the experimental data with a Lorentzian to extract its full-width-at-half-maximum (FWHM) of $1.1(1) \text{ MHz}$ and its center location $0.15(5) h\cdot\text{MHz}$ at finite energy mismatch. Both features are captured by the simulation, which yields a FWHM of 1 MHz and has its peak centered at $0.15 h\cdot\text{MHz}$ energy mismatch. Qualitatively, the calculation also captures the asymmetry of the experimental peak, which has a longer tail on the right side than the left side.

For pure contact interactions, the Laughlin state would not be shifted or broadened by interactions, and we anticipate that the collision resonance would be centered at an energy mismatch of zero and have a linewidth compatible with the non-interacting linewidth of two polaritons in the Laughlin state. However, the strong interactions in our system can shift and broaden the collision resonance. We attribute the width of the observed peak partially to the bare linewidth $0.6(1) \text{ MHz}$ of the non-interacting pair state [39] and partly to additional broadening due to interaction-induced loss of the photon pairs. Similarly, we attribute the slight offset of the peak from zero energy mismatch to the finite range of the interactions in our system. Alternative simulations performed with the opposite sign of C_6 cause the peak center to be shifted in the opposite direction. Moreover, simulations performed with a hypothetical hard-core Rydberg-Rydberg interaction potential ($U(r) = \infty$ for $r < 15 \mu\text{m}$, $U(r) = 0$ for $r \geq 15 \mu\text{m}$) yield a collision peak centered at an energy

mismatch of zero.

These observations are compatible with conservation of energy on a fundamental level, as indicated by the agreement of the experimental results with an energy conserving numerical calculation. They are also conceptually compatible with conservation of energy within the effective model of polaritonic quasiparticles, whose strong interactions can result in the total energy from the many-body Hamiltonian being conserved even when the energy from the individual particle component of that Hamiltonian is not conserved. Since the polaritons are sufficiently close to the limit of contact interactions that an energy mismatch of zero is well within the linewidth of the peak, we maintain the simple statement of energy conservation in the main text for clarity and accessibility.

As we move towards larger Laughlin states and more general filling factors, we anticipate it will be possible to incorporate the effect of finite-range interactions via higher-order Haldane pseudopotentials [83].

6. Understanding the Width of the Energy-Conservation Feature

One might wonder if the width of the energy conservation peak in Fig. 2c of the main text is actually set by the width of the EIT window rather than the requirement of energy conservation. That is: once the collision products are no longer within the EIT window, they will become lossy and will cease to be produced (a sort of *quantum zeno suppression* of collisions). The width of the cavity-EIT window is expected to be $\Gamma_{EIT} \approx \frac{\kappa}{2}\sqrt{N\eta} \approx 5 \text{ MHz}$, in the limit $G \gg \Omega$, which is substantially larger than the observed width of $\approx 1 \text{ MHz}$.

To verify this claim in numerical modeling, in Fig. S11 we compute and plot the rate of generating collision products versus $E_3 - E_6$ and $E_9 - E_6$, for our experimental parameters (enumerated in SI. B5). We find, as anticipated, a peak rate when $E_3 \approx E_9 \approx E_6$, surrounded by elliptical region of moderately high rate. If the EIT window were infinitely wide, this region would be infinitely elongated along the line $E_3 + E_9 = 2E_6$, with a finite width along the line $E_3 = E_6$ set by the degree to which energy must be conserved. What we observe is that the width along the former line is substantially larger than along the latter line, indicating that while the EIT window width is quite finite, the requirement that energy be conserved provides a more stringent limit and indeed is the primary driver of the width and shape of Fig. 2c.

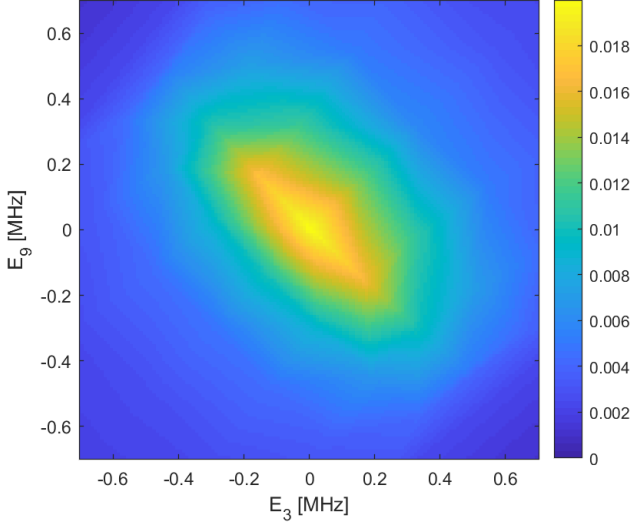


FIG. S11. Energy Conservation vs EIT Linewidth. To understand whether the width of the feature in Fig. 2c is dominated by energy conservation or the width of the EIT window, we perform atomistic numerics for the rate of forming collision products as a function of the quasi-energies E_3 and E_9 of the $l = 3, 9$ polaritons. For an infinitely wide EIT window, when $E_3 + E_9 = 2E_6$, collision products would be formed regardless of the value of $E_3 - E_6$ —that is, we would observe an infinitely long diagonal line running from the upper left to the lower right. That the collision product ellipse is finite along this axis indicates that we will eventually leave the EIT window; the fact that it is longer in this axis than the orthogonal axis indicates that energy conservation is a more strict requirement than the width of the EIT window.